FERROMAGNETIC SWITCHING OF KNOTTED VECTOR FIELDS

IN CHIRAL LIQUID CRYSTAL COLLOIDS

by

QIAOXUAN ZHANG

B.A., University of Colorado, 2013

A thesis submitted to the

Faculty of the Graduate School of the

University of Colorado in partial fulfillment

of the requirement for the degree of

Master of Science

Materials Science and Engineering Program

2015

This thesis entitled:
Ferromagnetic Switching of Knotted Vector Fields in Chiral Liquid Crystal Colloids
written by Qiaoxuan Zhang
has been approved for the Materials Science and Engineering Program

_____

Ivan I. Smalyukh

_____

Noel A. Clark

Date_____

The final copy of this thesis has been examined by the signatories, and we find that
both the content and the form meet acceptable presentation standards of scholarly
work in the above mentioned discipline.

Zhang, Qiaoxuan (M.S, Materials Science and Engineering)

Ferromagnetic switching of knotted vector fields in chiral liquid crystal colloids

Thesis directed by Associate Professor Ivan I. Smalyukh

We experimentally realize polydomain and monodomain chiral ferromagnetic liquid crystal colloids that exhibit solitonic and knotted vector field configurations. Formed by dispersions of ferromagnetic nanoplatelets in chiral nematic liquid crystals, these soft colloidal ferro-magnets exhibit spontaneous long-range alignment of magnetic dipole moments of individual platelets, giving rise to a continuum of magnetization field $\mathbf{M}(\mathbf{r})$. Competing effects of surface confinement and chirality prompt spontaneous formation and enable optical generation of localized twisted solitonic structures with double twist tubes and torus knots of $\mathbf{M}(\mathbf{r})$, which exhibit a strong sensitivity to direction and magnitude of weak magnetic fields of ~10 G. Numerical modeling, implemented through free energy minimization to arrive at field-dependent three-dimensional structures of $\mathbf{M}(\mathbf{r})$, shows a good agreement with experiments and provides insights into the corresponding physical underpinnings.

ACKNOWLEDGEMENT

CONTENTS

FIGURES

and (b) monodomain samples in an external magnetic field along $\mathbf{M}(\mathbf{r})$ in the toron center, obtained experimentally. $\mathbf{H}$ was turned on and off at times indicated by arrows in (b). The insets in (a) show corresponding polarizing micrographs of $\mathbf{H}$-tunable torons, with the white bar in the top-left one indicating the scale of 50 μm. Note that the concentration of magnetic nanoparticles in (b) is about 3 times of that in (a). (c,d) Similar characterization of A/A_0 but for $\mathbf{H}$ anti-parallel to $\mathbf{M}(\mathbf{r})$ in the toron center and parallel to that in its exterior for (c) polydomain and (d) monodomain samples. In a polydomain cell shown in (c), at a constant applied field, the toron first shrinks and then expands while shifting (marked by the white arrow in the bottom right insert) to get embedded in a domain with the background $\mathbf{M}$ opposite to that of the domain in which it was initially embedded. (e,f) Relative lateral toron area A/A_0 change vs. the absolute value of the magnetic field strength in a polydomain cell for two opposite vertical orientations of $\mathbf{H}$ for (e) polydomain and (f) monodomain samples probed experimentally and using numerical modeling. $\mathbf{H}$ is along and anti-parallel to $\mathbf{M}(\mathbf{r})$ in the toron for increasing ($A>A_0$) and decreasing ($A<A_0$) toron area, respectively

6.   Ferromagnetic switching of 2D solitons. (a) Relative change of the diameter of the double-twist-tube vs. time in $\mathbf{H}$ along the lateral $\mathbf{M}(\mathbf{r})$ on the axis of the double-twist-tube (positive in the plot), and field strength from 6.3G to 18.8G that is anti-parallel to $\mathbf{M}(\mathbf{r})$ on its axis (marked as negative in the plot), obtained experimentally. (b) Relative change of the overall width w/w_0 and diameter d/d_0 of the double-twist-tube within the transnationally invariant 2D soliton vs. absolute magnetic field strength. $\mathbf{H}$ is along and anti-parallel to $\mathbf{M}(\mathbf{r})$ on the double-twist tube axis for $w>w_0$ (or $d>d_0$) and $w<w_0$ (or $d<d_0$), respectively. The strength of coupling of $\mathbf{M}(\mathbf{r})$ with $\mathbf{H}$ in computer simulations was calibrated using the experimental field strength and magnitude of the magnetic moment of the system, which is related to the concentration of

CHAPTER I

INTRODUCTION

Envisaged in early works of Gaus, Kelvin, and Tait [1], linking and knotting of closed loops in physical field lines can be finally controllably realized and experimentally probed [2-9]. For example, liquid crystals (LCs) permit both nonsingular solitonic structures with knotting and linking of loops in the nonpolar molecular alignment field $\mathbf{n(r)}$ [3,7,9] and also loops of singular linear vortices along which this orientational ordering vanishes [5,6]. Knots and links have been experimentally realized in electromagnetic fields [2], optical vortices [8], solid colloidal particles [6], and fluid flows [4], while physical systems with such field configurations predicted theoretically include subatomic particles, Bose-Einstein condensates, various ferromagnets, and cosmology [10-16]. In different ferromagnetic systems [17], torus knots of magnetization field are expected to form three-dimensional (3D) topological solitons labeled by elements of the third homotopic group $\pi_3(S^2)=Z$ [13-16], similar to their nematic counterparts $\pi_3(RP^2)=Z$ [3,7,9], but realized in magnetization $\mathbf{M(r)}$ vector field rather than molecular alignment line field $\mathbf{n(r)}$. However, such 3D solitons in $\mathbf{M(r)}$ have not been observed so far, despite the fact that their two-dimensional solitonic counterparts, which are labeled by elements of the second homotopic group $\pi_2(S^2)=Z$, are relatively abundant and recently attract a great deal of interest [18,19].

In this work, we experimentally realize chiral ferromagnetic liquid crystal colloids (CFLCCs) with solitonic and knotted $\mathbf{M(r)}$-configurations, which form in relatively dilute ordered dispersions of ferromagnetic nanoplatelets in a chiral nematic liquid crystal [20]. The competition of medium's chirality with the strong surface anchoring at bounding substrates that suppresses realization of unidirectionally twisted structures in CFLCCs prompts spontaneous formation of localized twisted solitonic structures with double twist tubes and torus knots of $\mathbf{M(r)}$, which are $\pi_2(S^2)=Z$ and $\pi_3(S^2)=Z$ topological solitons, respectively. They exhibit a strong polar response to weak magnetic fields and are accompanied by hyperbolic point defects of opposite hedgehog charge. Numerical free energy minimization yields 3D $\mathbf{M(r)}$-structures that match their experimental counterparts and reveal topologically protected particle-like configurations that resemble famous mathematical Hopf fibration and topological solitons dubbed "hopfions" theoretically predicted to exist in many branches of physics [1,3,7,9,21].

CHAPTER II

MATERIALS AND METHODS

Sample Preparation

Barium hexaferrite nanoplatelets with the chemical composition $BaFe_{11}CrO_{19}$ were synthesized by thermohydrodrate method [22] using chemical ingredients $Fe(NO_3)_3 \cdot 9H_2O$, $Cr(NO_3)_3 \cdot 9H_2O$, $Ba(NO_3)_2$ and NaOH purchased from Alfa Aesar. Briefly, in a 25 mL teflone-lined-autoclave, 0.01 M of $Ba(NO_3)_2$, 0.04 M of $Fe(NO_3)_3$ and 0.01 M of $Cr(NO3)_3$ according to the nominal stoichiometry were dissolved in de-ioned (DI) water and co-precipitated by 2.72 M of NaOH with the final volume of 20 mL. The resultant material was hydrothermally heated to 220 °C at a rate of 3 °C/min and naturally cooled down to the room temperature. The powders were washed with nitric acid and acetone and re-dispersed in 1 mL water. The thickness of the synthesized magnetic platelets was about 10 nm while the average diameter was about 105 nm (determined from TEM images) [22]. The magnetic nanoplatelets were then functionalized by polymer to increase their stability in the nematic host. For this, 100 mL of nanoplatelets solution were added to 10 mL DI water and the pH was adjusted to be within 3-4. 1 mL of ethanol solution with 20 mg of 5 kDa silane-terminated polyethylene glycol (silane-PEG) was added to nanoparticle solution drop-by-drop. The silane group was hydrolyzed and linked to OH group at the surface of nanoplatelets. The magnetic nanoplatelet dispersion was then left for

overnight, followed by centrifugation at 14.6k for 30 min and washing by ethanol twice.

To prepare CFLCCs, 15 µL of pentylcyanobiphenyl (5CB) was dissolved in 15 µL ethanol and mixed with ~10 µL of magnetic nanoplatelets dispersed in ethanol and then the ethanol was fully evaporated while the sample was kept at 90 °C for 3 hours, yielding an excellent dispersion in the isotropic phase at no applied fields. The sample was quenched down to the nematic phase of 5CB while vigorously stirring. The ensuing CFLCC was centrifuged at 2200 rpm for 5 min to remove residual aggregates, so that the final composite contained only well-dispersed nanoparticles. The dispersion was then additionally doped with a chiral agent cholesteryl nonanoate to define the equilibrium cholesteric pitch $p=1/(hC_{CN})$, distance over which $\mathbf{M(r)}$ ∥ $\mathbf{n(r)}$ of the equilibrium-state CFLCC rotates by 360°, where h=6.25 mm^{-1} is helical twisting power and C_{CN} is concentration of cholesteryl nonanoate. Magnetic platelets with silane-PEG functionalization exhibited spontaneous alignment with large-area faces orthogonal to $\mathbf{n(r)}$, which we tested by measuring polarization-dependent absorbance in planar cells (Fig. 1a) and probing response of their dilute dispersions in 5CB to applying magnetic fields parallel and orthogonal to $\mathbf{n(r)}$. Liquid crystalline dispersions of ferromagnetic nanoplatelets were stable at applied magnetic fields of up to 200G, exhibiting facile response to low fields of the order of 10G. Homeotropic glass cells with polydomain CFLCCs having $\mathbf{M(r)}$ pointing along one of the two anti-parallel directions along the vertical far-field director $\mathbf{n}_0$ were prepared using 1 or 0.15 mm

thick glass plates treated with an aqueous solution of N,N-dimethyl-N-octadecyl-3-aminopropyl-trimethoxysilyl chloride (DMOAP) via dip-coating to set surface boundary conditions for the director perpendicular to substrates. Alternatively, polyamide SE1211 (from Nissan Chemicals) alignment layers were prepared via spin coating and baking at 185 °C for 1 h. To define monodoman CFLCCs with the same orientation of the far-field magnetization vector M_0, magnetic nanoplatelets were added to the polyamide and spin coating was done in presence of magnetic field (~400 G) normal to the glass plate provided by a permanent magnet underneath it. Assuring like-orientation of the easy axes for M_0 at the inner surfaces of the two confining cell plates, we thus defined ferromagnetic monodomains within typically inch-wide homeotropic CFLCC cells. The cell thickness between substrates was set to be ~60 µm using UV curable optical adhesive (NOA-65, from Norland Products) with dispersion of spherical silica spacers of 60 µm diameter. The pitch of CFLCC, a distance over which liquid crystal molecules and nanoplatelet normal twist by 2p, was set as p=70 µm by setting the concentration of the chiral agent in the sample to be C_{CN}=0.229 w%. After infusing CFLCCs into polydomain or monodomain cells, we performed magnetometer experiments (Fig. 1) using an alternating gradient magnetometer (MicroMag 2900, from Princeton Measurement Corporation). Unlike non-chiral nematic dispersions of the same nanoplatelet dispersions in 5CB without the chiral additive (Fig. 1d), CNLCC cells with solitonic structures exhibit magnetic hysteresis loops not only at $H \parallel n_0$ but also at

H⊥**n**$_0$ (Fig1b,c).
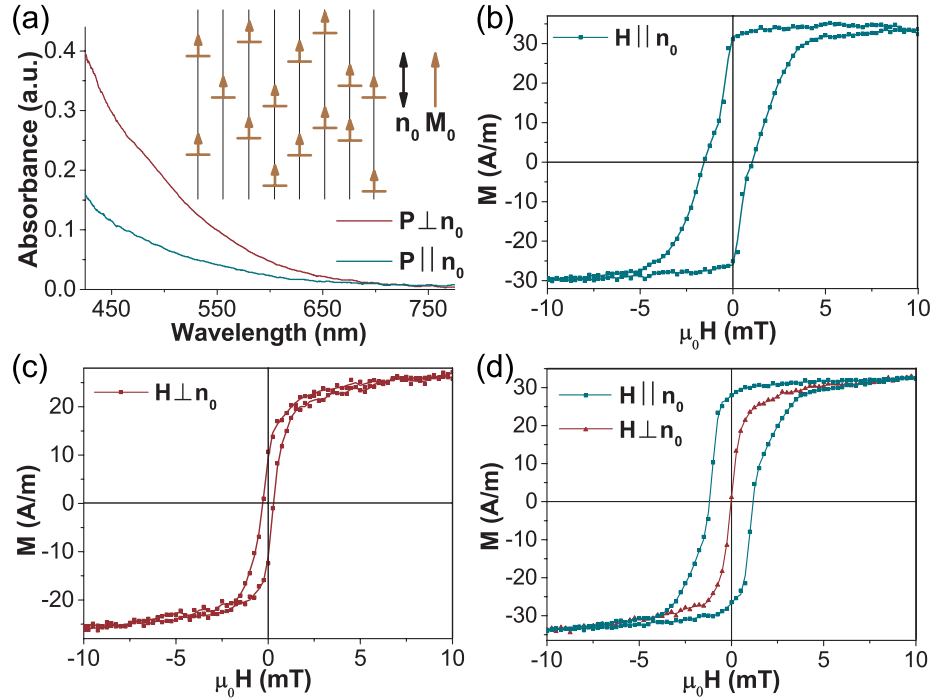
FIG. 1. Characterization of CFLCCs. (a) Optical absorbance at incident light polarizations **P**∥**n**$_0$ and **P**⊥**n**$_0$ obtained using a 60 µm thick cell with the CFLCC formed by self-aligned nanoplatelets dispersed in 5CB, as schematically shown in the inset. (b-d) Magnetic hysteresis loops for a monodomain CFLCC containing solitonic structures with (b) **H**∥**n**$_0$ and (c) **H**⊥**n**$_0$; (d) similar data for a ferromagnetic monodomain of nanoplatelet dispersion in 5CB without a chiral additive.

Experimental System

We use an integrated holonomic magnetic and a holographic optical manipulation system, as shown in Fig. 2 [24]. Magnetic manipulation is achieved by a three-axis electromagnetic apparatus formed by solenoids (Fisher Scientific International, Inc. S52051 air-core solenoids with custom machined cast iron cores). The solenoids are arranged in a Cartesian frame, machined from aluminum, and

mounted directly on the microscope body. Each electromagnet is independently driven via an amplified power supply (APS, model BOP20-5M, from Kepco), which is voltage controlled by a computer-controlled data acquisition (DAQ) card (National Instruments USB-6259 BNC) and in-house LABVIEW-based software (LABVIEW was obtained from National Instruments). In some circumstances, an ancillary Helmholtz coil driven by a dc current source is used for high gradient magnetic-field pitch control, depth-resolved translation of defects, or to null magnetic-field gradients. Using precision translation stages, an aluminum microscope slide holder is positioned on the x-y plane. The aluminum frame also acts as a heat sink, enabling the electromagnets to ambient-air cool, and therefore, the samples is not heated over several hours of continuous operation. Each electromagnet can produce ac (up to 8 Hz) and/or dc magnetic fields up to 100 G as measured at the sample by a Gauss meter. This field affects all the sample volume simultaneously, which enables instantaneous ferromagnetic switching of the microstructures in the CFLCC sample. The low magnetic field has no significant direct coupling between the magnetic field and the LC molecules when assuring robust control of ferromagnetic and super paramagnetic particles. Since most know LCs, including the one used in this project, are diamagnetic materials, director realignment by magnetic field is typically a threshold-like effect, which require field strength in the scale of 1 T. Therefore, the magnetic fields used in our experiments to realigning magnetic nanoparticles have negligible influence on LC director itself.
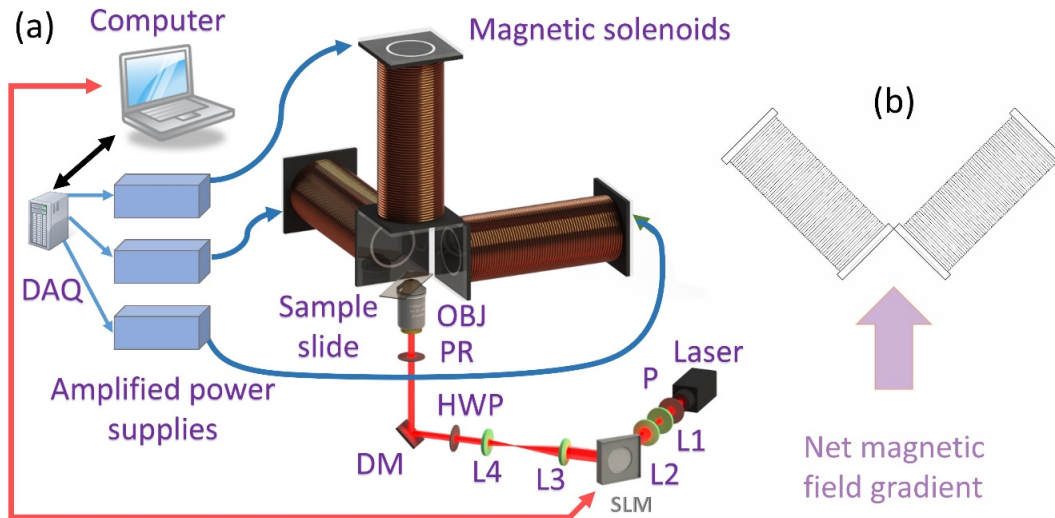
FIG. 2. Integrated holonomic magnetic and holographic optical manipulation system. (a) Electromagnetic solenoids arranged on a Cartesian aluminum frame mounted on an inverted microscope (not shown). The solenoids are driven by amplified power supplies via computer controlled DAQ. The HOT is based on a fiber laser and an optical setup with the following optical elements: polarizer (P), lenses of two telescopes (L1, L2, L3, L4), computer controlled, dynamically addressable liquid crystal based spatial light modulator (SLM), a 100x oil immersion objective (OBJ), half wave plate (HWP), polarization rotator (PR) and a dichroic mirror (DM). The trapping beam is focused within the sample volume. This manipulation setup is integrated with an optical imaging system capable of both POM and 3PEF-PM imaging. (b) Two solenoids arranged in the *xy*-plane aligned with the microscope's focal plane. The direction of the net magnetic force due to magnetic field gradients in this configuration is shown by the arrow.

Although the used solenoids are designed to minimize magnetic gradient forces within the sample volume, their cores have a finite radius and geometric arrangement which results in a residual in-plane fringe field gradient which can yield residual forces acting on the magnetic nanoparticles in the sample [24]. This gradient force is directed along the y-axis (in a two solenoid configuration), as shown by an arrow in Fig. 2b.

Optical microscopy observations were performed using an inverted polarizing

optical microscope (POM) (Olympus IX81) with a 10x or 4x air objective. Optical video microscopy was used to probe ferromagnetic switching of topological solitons through recording their motion with a charge coupled device camera (Flea, PointGrey) and then determining their time dependent sizes and shapes from captured image sequences using imageJ by applying a certain threshold to the red channel of the original RGB images.

CHAPTER III

RESULTS

Confined CFLCCs and Topology of 2D and 3D solitons

CFLCC cells with vertical surface boundary conditions for $\mathbf{n}_0$ without selection of one of the two anti-parallel $\mathbf{M} \| \mathbf{n}_0$ orientations are poly-domain in nature (Fig. 3a-f), with domains of opposite $\mathbf{M}_0$ separated by walls "invisible" at no fields (Fig. 3a), but apparent in magnetic fields applied in different directions (Fig. 3c-f). The lateral size of these magnetic domains is typically 2-3 times that of the cell gap thickness. In monodomain samples (Fig. 3g,h), the magnetization alignment layers define the same orientation of $\mathbf{M}_0$ everywhere in an inch-wide cell. These monodomain samples show no response at $\mathbf{H} \| \mathbf{M}_0$ but exhibit a facile response to fields at all other orientations, including when they are anti-parallel to $\mathbf{M}_0$. Similar to chiral nematic liquid crystals without dispersed nanoplatelets, CFLCCs can host deliberately generated or naturally occurring solitonic structures, such as torons, hopfions, and fingers [3,7,9, 23], which in polydomain samples can be fully embedded within a single domain of the same orientation of the surrounding $\mathbf{M}$ or span across two or more domains. Since dimensions of such solitonic structures are at least three orders of magnitude larger than the size of magnetic nanoplatelets, mechanical coupling of platelets through surface anchoring boundary conditions forces the platelets to orient orthogonally to $\mathbf{n}(\mathbf{r})$ (inset of Fig. 1a) [20], so that $\mathbf{M}(\mathbf{r})$ is continuous and follows the

molecular alignment field $\mathbf{M}(\mathbf{r})$ ∥ $\mathbf{n}(\mathbf{r})$ everywhere within the interior of these topological solitons. Consistent with the results of three-dimensional (3D) nonlinear optical imaging of $\mathbf{n}(\mathbf{r})$, similar to that reported elsewhere [7,9], numerical models of $\mathbf{M}(\mathbf{r})$ ∥ $\mathbf{n}(\mathbf{r})$ reveal both 2D and 3D twisted topological solitons resembling cholesteric fingers (Fig. 4a,b) as well as torons containing hopfions with knotted solitonic $\mathbf{M}(\mathbf{r})$ accompanied by point defects (Fig. 4c-f). The cross-section of the translationally invariant 2D CFLCC soliton is composed of a double twist tube, similar to that of 2D baby schyrmions in atomic chiral ferromagnets [18,19], accompanied by a nonsingular meron-like anti-skyrmion structure (Fig. 4a) [18,19]. Projection of $\mathbf{M}(\mathbf{r})$ from this cross-section onto the order parameter space, an S^2-sphere, covers the sphere once (Fig. 4b), implying an elementary skyrmion number of this solitonic field configuration. An equatorial cross-section of the 3D solitonic structure resembles a 2D skyrmion too (Fig. 4c) and $\mathbf{M}(\mathbf{r})$ within this cross-sections also covers the S^2-sphere once (Fig. 4d). However, by numerically following $\mathbf{M}(\mathbf{r})$ field lines from a representative set of points of this equatorial plane corresponding to a dashed circle marked on the S^2-sphere in Fig. 4d, we find that $\mathbf{M}(\mathbf{r})$ field lines close into circular loops, all of which are linked with each other and   define a surface of torus (Fig. 4d), like in the mathematical Hopf fibration and in solitonic field configurations of "hopfions" [9]. The closed loops of $\mathbf{M}(\mathbf{r})$ are linked with each other once, defining the so-called Hopf index of the knotted soliton Q_H=1 [1,9]. Close to the confining surfaces (Fig. 4e), one also finds two hyperbolic point defects of opposite hedgehog charge, similar to

the ones previously observed in **n**(**r**) the toron structures of chiral nematics [3].
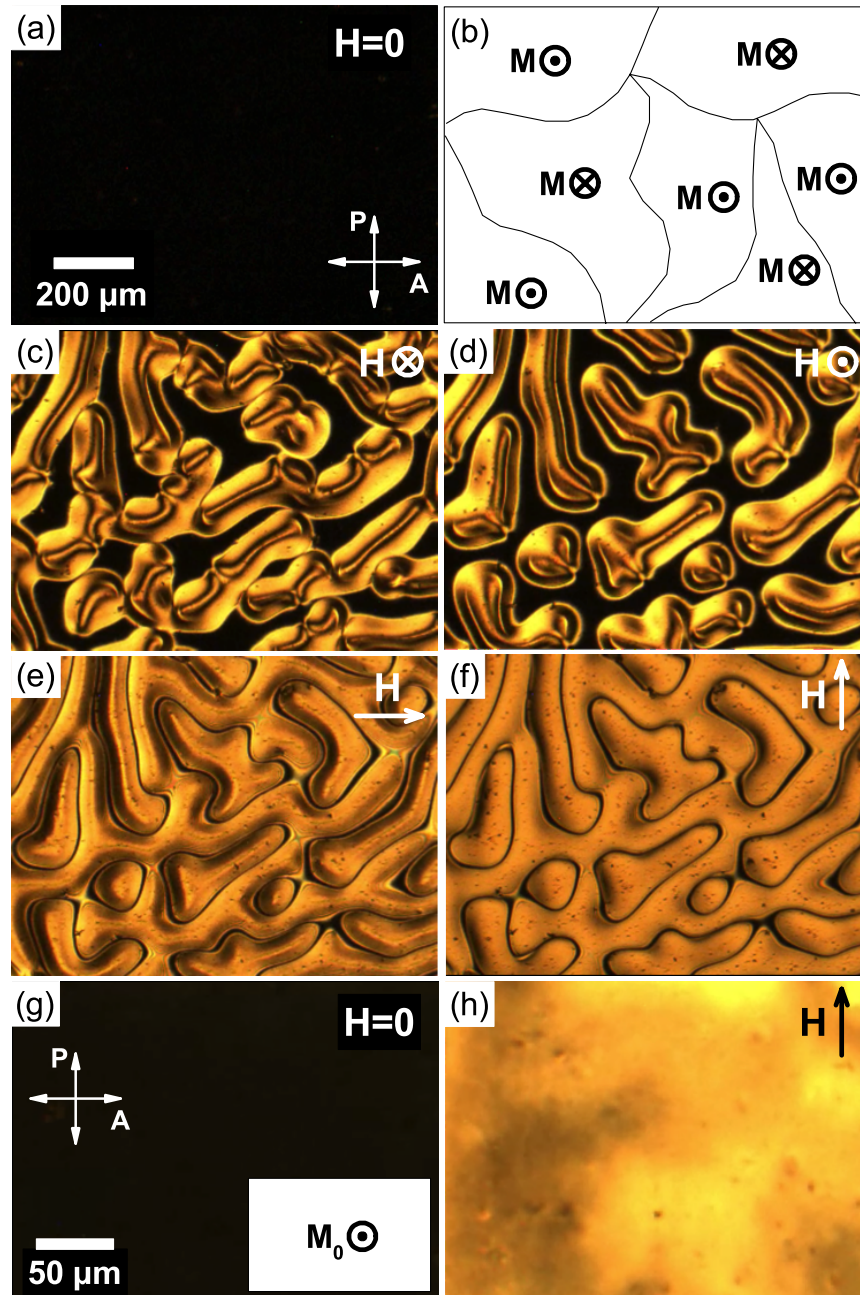
FIG. 3. Polydomain and monodomain confined CFLCCs in homeotropic CFLCC cells with $p \approx 70$ μm and cell gap thickness ~60 μm. (a) A polarizing optical micrograph of a polydomain cell at no fields. (b) Schematics of domain distribution in such a polydomain cell. (c-f) Polarizing optical micrographs of the same cell in an external magnetic field directed as marked on images. (g,h) Polarizing optical micrographs of the CFLCC in a monodomain cell (g) at no external fields (remains intact at **H** along **M**$_0$) and (h) at **H** directed as marked by an arrow. The bottom-right insert in (g) schematically shows the single magnetic domain of the entire cell. The applied field was ~60 G.
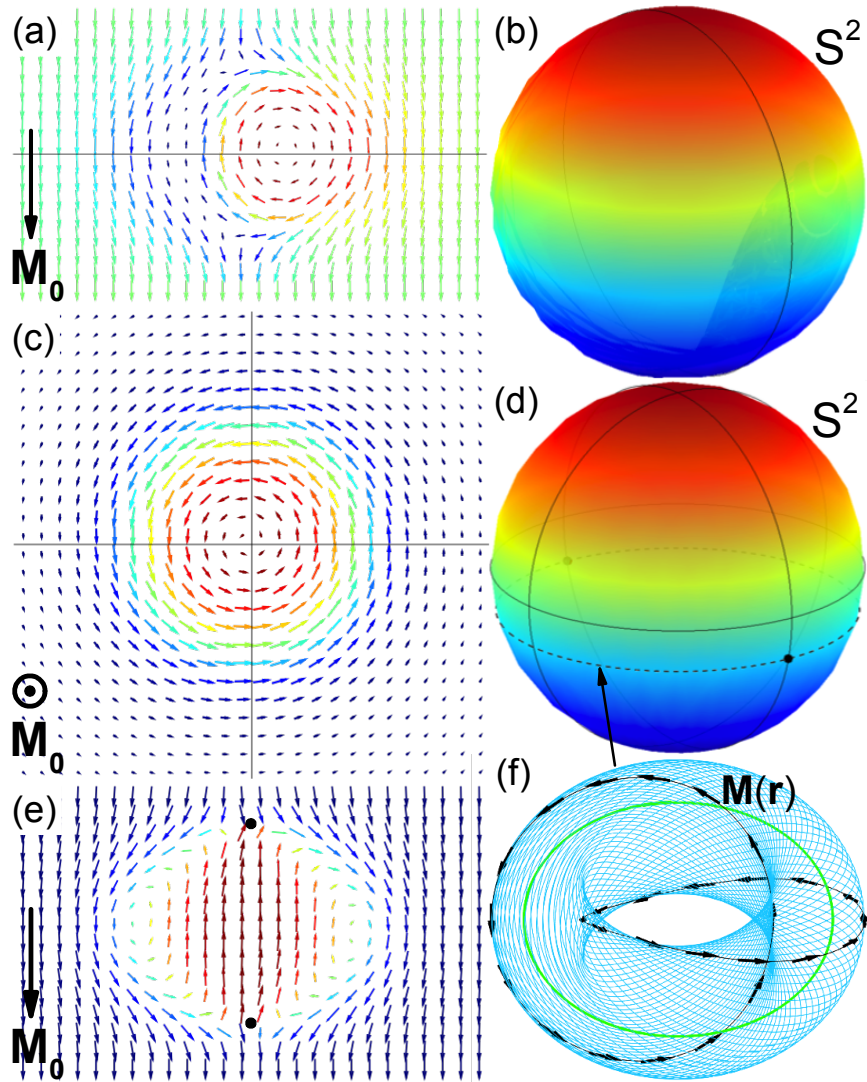
FIG. 4. Topology of 2D and 3D CNLCC solitons. (a,b) Numerically simulated (a) cross-section of a translationally invariant 2D solitonic structure of **M**(**r**) shown using arrows, with the colors depicting vector orientations correlated with points on the order parameter space, the S^2-sphere shown in (b). The black circle in (b) corresponds to the continuous change of **M**(**r**) orientation along the horizontal black line in (a). (c) An in-plane cross-section of the 3D solitonic structure passing through the cell midplane. (d) The corresponding map of **M**(**r**) orientations shown on the S^2-sphere, with the two vertical black circles corresponding to the straight black lines shown in (c) and the circle at the equator of the sphere representing a region of the solitonic structure in (c) within which **M**(**r**) is parallel to the cell substrates. (e) A vertical cross-section of the toron structure obtained along the horizontal line shown in (c); black filled circles mark the hyperbolic point defects. (f) A torus surface formed by a dense series of inter-linked closed loops of **M**(**r**) corresponding to a dashed circle shown in (d) and marked by an arrow. Two representative closed loops of **M**(**r**), corresponding to black points on the opposite sides of the S^2-sphere shown in (d), are highlighted by black arrows indicating local **M**(**r**) orientation. The green circular axis of the torus corresponds to the equatorial circle shown in (d).

Ferromagnetic Switching of Torons

CFLCC solitons exhibit a facile response to magnetic fields, which is highly dependent on the field orientation (Figs. 5 and 6). In both monodomain and polydomain samples, the lateral size of 3D topological solitons increases when **H** is along the vertical **M(r)** in the toron center and anti-parallel to that in its exterior (Fig. 5a,b). Torons in monodomain samples (Fig. 5d) and some torons in polydomain samples shrink when **H**-orientation is reversed, until eventually disappearing at some critical field (Fig. 5e,f). However, some torons in polydomain samples exhibit a more complex behavior at **H** anti-parallel to **M(r)** in their interior (Fig. 5c), shrinking in size for some time and then shifting to a near-by domain of opposite magnetization and expanding similar to torons in domains with **H** along the vertical **M(r)** in the toron center. In all samples, the response to **H** is threshold-free (because of the existence of a pre-distorted field configuration), but relatively slow, consistent with the fact that the toron size and cell thickness are large (Fig. 5). Upon turning the field off, torons always relax to the initial equilibrium lateral size (Fig. 5a-d), unless the field applied to an irreversibly shrinking toron exceeds some critical value (dependent on nanoplatelet concentration), at which the lateral size of torons abruptly changes discontinuously when the entire solitonic structure disappears during a discontinuous re-configuration of **n(r)**. The lateral diameter of torons cannot be shrink below ~0.5 of its equilibrium value at H=0, and forcing it below this size causes discontinuous size jump (Fig. 5e,f) accompanied by a complex transition from the initial knotted to a
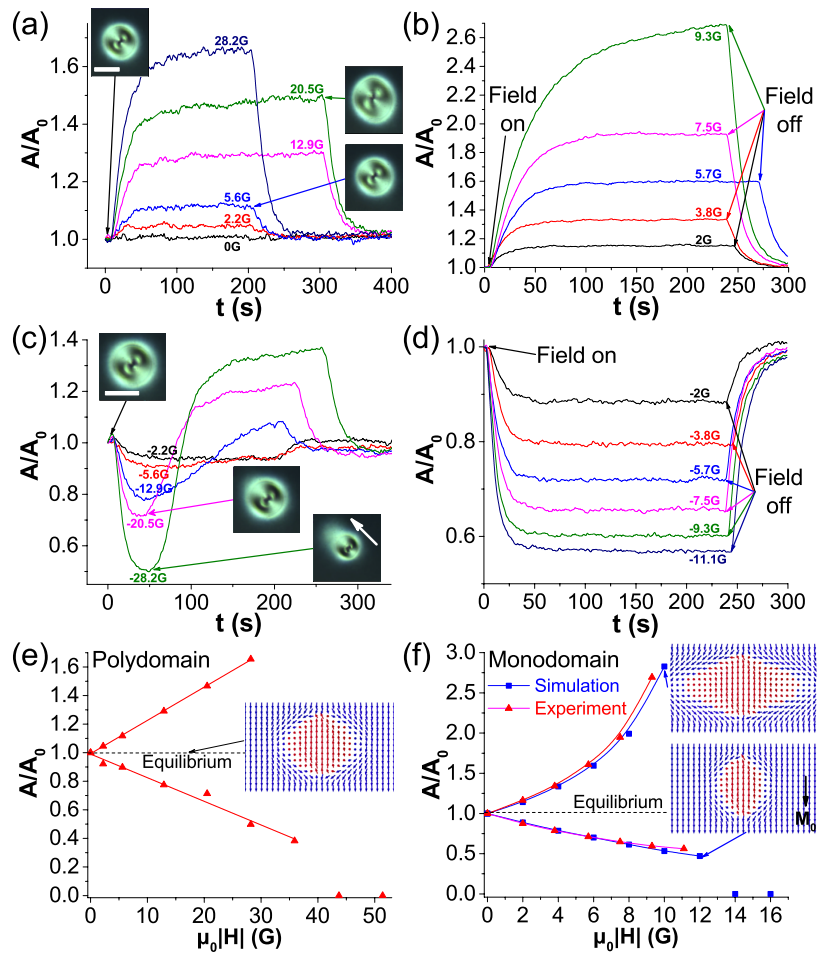
uniform field configuration.

FIG. 5. Ferromagnetic switching of torons. (a, b) Relative lateral toron area A/A_0 changes vs. time in (a) polydomain and (b) monodomain samples in an external magnetic field along $\mathbf{M(r)}$ in the toron center, obtained experimentally. $\mathbf{H}$ was turned on and off at times indicated by arrows in (b). The insets in (a) show corresponding polarizing micrographs of $\mathbf{H}$-tunable torons, with the white bar in the top-left one indicating the scale of 50 μm. Note that the concentration of magnetic nanoparticles in (b) is about 3 times of that in (a). (c,d) Similar characterization of A/A_0 but for $\mathbf{H}$ anti-parallel to $\mathbf{M(r)}$ in the toron center and parallel to that in its exterior for (c) polydomain and (d) monodomain samples. In a polydomain cell shown in (c), at a constant applied field, the toron first shrinks and then expands while shifting (marked by the white arrow in the bottom right insert) to get embedded in a domain with the background $\mathbf{M}$ opposite to that of the domain in which it was initially embedded. (e,f) Relative lateral toron area A/A_0 change vs. the absolute value of the magnetic field strength in a polydomain cell for two opposite vertical orientations of $\mathbf{H}$ for (e) polydomain and (f) monodomain samples probed experimentally and using numerical modeling. $\mathbf{H}$ is along and anti-parallel to $\mathbf{M(r)}$ in the toron for increasing ($A>A_0$) and decreasing ($A<A_0$) toron area, respectively.

Ferromagnetic switching of 2D solitons

Switching of the 2D solitons is also orientation-dependent (Fig.6). The double-twist-tube part of these solitons expands when **H** matches **M(r)** on its axis but shrinks in the anti-parallel case, with the corresponding changes of the overall width of these solitons (Fig. 6). This behavior is natural as the linear coupling term of free energy is minimized in the respective cases, consistent with the outcomes of our numerical modeling (Fig. 6b,c). The **H**-field prompts expansion of soliton's regions co-linear with **H** and shrinking of cell regions with **M(r)** anti-parallel to **H**. The presence of 2D and 3D solitonic structures with a uniform surrounding M_0 explains observation of the magnetic hysteresis curves in this system even at $H \perp n_0$ (Fig. 1c), which is due to the soliton interior regions with local $M(r) \| n(r)$ orthogonal to M_0.
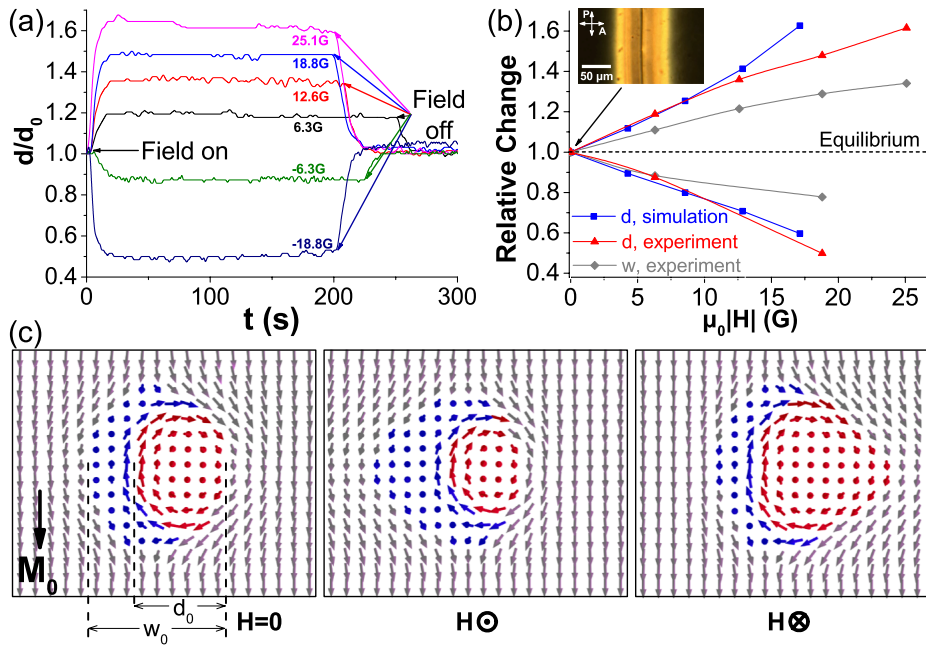

FIG. 6. Ferromagnetic switching of 2D solitons. (a) Relative change of the diameter of the double-twist-tube vs. time in **H** along the lateral **M(r)** on the axis of the double-twist-tube (positive in the plot), and field strength from 6.3G to 18.8G that is anti-parallel to **M(r)** on its axis (marked as negative in the plot), obtained experimentally. (b) Relative change of the overall width w/w_0 and diameter d/d_0 of the double-twist-tube within the transnationally invariant 2D soliton vs. absolute magnetic field strength. **H** is along and anti-parallel to **M(r)** on the double-twist tube axis for $w>w_0$ (or $d>d_0$) and $w<w_0$ (or $d<d_0$), respectively. The strength of coupling of **M(r)** with **H** in computer simulations was calibrated using the experimental field strength and magnitude of the magnetic moment of the system, which is related to the concentration of magnetic nanoparticles of the CNLCC. (c) Computer simulated cross-sectional side views of the transnationally invariant 2D soliton at no external fields (left), **H** pointing into the screen (middle), and **H** pointing out of the screen (right), respectively.

Close examination of the cross-section shown in Fig. 4e indicates that the double torus of $\mathbf{M}(\mathbf{r})$ cannot be easily matched to the uniform far field in the surrounding without introducing point defects, such as the two ±1 point defects above and below it nearby the confining substrates. This is different from the topology of the $\mathbf{n}(\mathbf{r})$ line field of torons and hopfions [7,9], in which case hopfion field configurations without point defects are possible.

Interestingly, unlike electrically induced patterns in confined chiral nematic liquid crystals, which exhibit typical liquid crystal switching dynamics, magnetically induced patterns in CFLCCs exhibit very slow relaxation back to the initial uniform state. This relaxation can take hours. As an example, we show a periodic stripe pattern induced from an initially uniform unwound CFLCC state (Fig. 7a,b), which can take an hour or so to fully relax. We attribute this observation to ferromagnetism of CFLCCs. Future studies will need to explore physical underpinnings of this interesting observation.
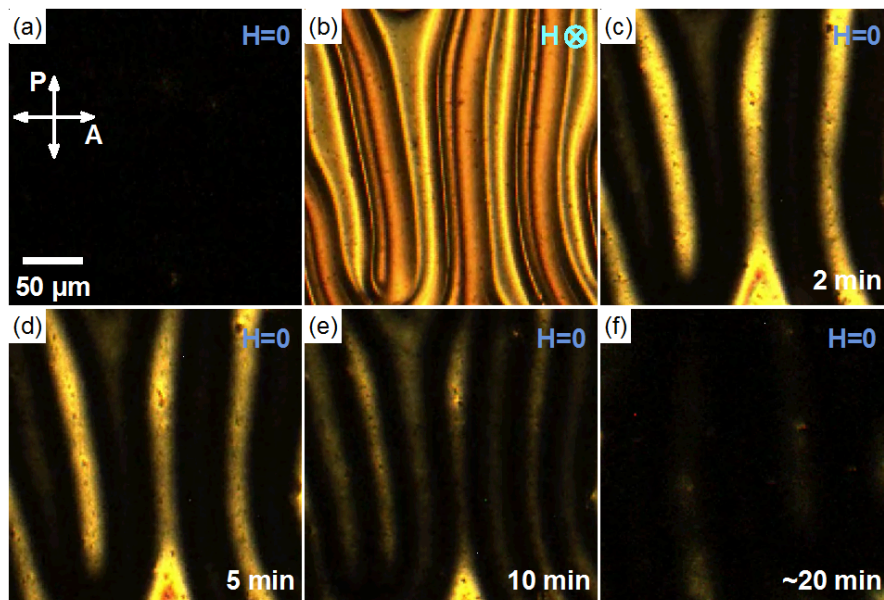
FIG. 7. Long-term stripe pattern relaxation. (a-f) Polarizing optical micrographs obtained (a) before field is applied, (b) when field is applied, (c) 2 min after field is switched off, (d) 5 min after field is switched off, (e) 10 min after field is turned off, (f) ~20 min after field is switched off (in a slightly different region right next to the region in (a-e)). The elapsed time after the field is turned off is also marked on images in the bottom right corners.

CHAPTER IV

CONCLUSION

To conclude, we have experimentally realized and numerically modeled 2D skyrmionic and 3D knotted magnetization vector field configurations in a novel soft matter system of CNLCCs. We have also demonstrated ferromagnetic switching of such twisted and knotted solitons. Although knotted solitons (hopfions) have been recently controllably and abundantly generated in frustrated chiral nematic liquid crystals, these solitons exist in a non-polar line field and, to the best of our knowledge, the knotted field configurations demonstrated in this study are the first such experimental realizations for the magnetization vector field. The experimental platform we have developed may allow for probing topological transformation of solitonic field configurations driven by weak external stimuli, with potential uses ranging from modeling similar phenomena in other branches of physics, such as particle physics and cosmology, to practical applications in magneto-optic devices.

REFERENCES

1. L. H. Kauffman. *Knots and Physics* (World scientific, Singapore, 2001).

2. W. T. Irvine and D. Bouwmeester. *Nature Phys.* **4**, 716-720 (2008).

3. I. I. Smalyukh, Y. Lansac, N. A. Clark, and R. P. Trivedi. *Nature Mater.* **9**, 139-145 (2010).

4. D. Kleckner, and W. T. Irvine. *Nature Phys.* **9**, 253-258 (2013).

5. U. Tkalec, M. Ravnik, S. Čopar, S. Žumer, and I. Muševič. *Science*, *333*, 6038, 62-65 (2011).

6. A. Martinez, M. Ravnik, B. Lucero, R. Visvanathan, S. Žumer, and I. I. Smalyukh. *Nature Mater. 13*, 258-263 (2014).

7. B. G. Chen, P. J. Ackerman, G. P. Alexander, R. D. Kamien, and I. I. Smalyukh. *Phys. Rev. Lett.* **110**, 237801 (2013).

8. M. R. Dennis, R. P. King, B. Jack, K. O'Holleran, and M. J. Padgett. *Nat. Phys.* **6**, 118-121 (2010).

9. P. J. Ackerman, J. van de Lagemaat, and I. I. Smalyukh. *Nature Comm.* **6**, 6012 (2015).

10. A. F. Ronada, J. L. Trueba J L. *Nature* **383**, 32 (1996).

11. Y. Kawaguch, M. Nitta, M. Ueda. *Phys. Rev. Lett.* **100**, 180403 (2008).

12. Y. K. Liu, C Zhang, and S. J. Yang. *Phys. Lett. A* **377**, 3300–3303 (2013).

13. N. R. Cooper. *Phys. Rev. Lett.* **82**, 1554-1557 (1999).

14. P. Sutcliffe. *Phys. Rev. B* **76**, 184439 (2007).

15. A. B. Borisov, F. N. Rybakov. *JETP Lett.* 90:544–547.

16. L. Faddeev, and A. Niemi.. *Nature* **387**, 58-61 (1997).

17.   P. M. Chaikin, T. C. Lubensky. *Principles of condensed matter physics*. (Cambridge University Press, Cambridge, 1995).

18.   U. K. Rößler, A. N. Bogdanov, and C. Pfleiderer. *Nature* **442**, 797-801 (2006).

19.   S. Mühlbauer, B. Binz, F. Jonietz, C. Pfleiderer, A. Rosch, A. Neubauer, R. Georgii, and P. Böni. *Science* **323**, 915-919 (2009).

20.   A. Merte, D. Lisjak, M. Drofenik, M. Čopič. *Nature **504***, 237-241 (2013).

21.   H. Hopf. *Selecta Heinz Hopf* (Springer Berlin Heidelberg, German, 1964).

22.   D. Lisjak and M. Drofenik. *Cryst. Growth Des.* **12**, 5174-5179 (2012)

23.   P. Oswald, J. Baudry, and S. Pirkl. *Phys. Rep.* **337**, 67-96 (2000).

24.   M. C. M. Varney, N. J. Jenness, and I. I. Smalyukh. *Phys. Rev. E* **89**, 022505 (2014).